Tectonophysics 815 (2021) 228994

Contents lists available at ScienceDirect

Tectonophysics

journal homepage: www.elsevier.com/locate/tecto

Influence of in-situ temperatures and pressures on the permeability of hydrothermally altered basalts in the oceanic crust

Alannah C. Brett-Adams [a,*], Larryn W. Diamond [a], Claudio Petrini [b,1], Claudio Madonna [b]

[a] Institute of Geological Sciences, University of Bern, Baltzerstrasse 1+3, 3012, Switzerland
[b] Structural Geology and Tectonics Group, Geological Institute, Department of Earth Sciences, ETH Zurich, Sonneggstrasse 5, 8092 Zurich, Switzerland

ARTICLE INFO

Keywords:
Permeability
High temperature experiments
Hydrothermally altered basalt
Spilite
Epidosite
Seafloor

ABSTRACT

Hydrothermal circulation through oceanic crust, and all the transfers of mass and heat caused by this circulation, are controlled by the evolving permeability of the altered basaltic rocks at in-situ pressures (*P*) and temperatures (*T*). Numerical models designed to elucidate these processes therefore rely on knowledge of the rock-matrix permeabilities as a function of *P* and *T* and degree of hydrothermal alteration. We provide the first measurements of changes in permeability of two major types of high-temperature alteration of basalts, i.e., spilites and epidosites, over the *P–T* range relevant to hydrothermally active oceanic crust. Experiments were performed on microfracture-poor samples of pervasively altered pillow lavas and sheeted dikes from the Semail (Oman) and Troodos (Cyprus) ophiolites. Gas permeameter measurements at room temperature show that compression to ~55 MPa effective pressure reduces the permeabilities of spilites and epidosites by approximately ~80%. Measurements at 50 MPa effective pressure using an oscillating flow apparatus show that heating spilites and epidosites from 25 to 450 °C reduces their permeabilities by ~40% and 50%, respectively. SEM observations before and after the experiments rule out formation of new microfractures. The small reduction in permeability upon heating is attributed to closure of the sparse pre-existing microfractures (> 200 μm) due to thermoelastic expansion of the crystalline matrix combined with local restriction of throats between interstitial pores due to anisotropic mineral expansion. Temperature cycling demonstrates that these changes in permeability are reversible. Duplicate measurements on cores drilled from the same rock samples reveal that all these effects are small compared to the natural heterogeneity of permeability in spilites and epidosites at the centimeter scale. Nevertheless, our quantitative temperature–permeability correlations at subseafloor pressures allow the changes in permeability for these alteration types to be incorporated into numerical simulations of water–rock interaction in the oceanic crust.

1. Introduction

Quantitative understanding of how seawater infiltrates magmatically heated oceanic crust and develops hydrothermal circulation cells requires knowledge of the permeability of the basaltic rock-matrix and the fracture networks (Fisher, 1998; Hasenclever et al., 2014). Previous laboratory measurements of permeability have been performed on oceanic basalts that are hydrothermally unaltered ("fresh") or that show weak, low-temperature hydrothermal alteration consisting of clay- and zeolite-bearing mineral assemblages (Gilbert and Bona, 2016; Jarrard et al., 2003; Johnson, 1980; Karato, 1983). These experiments have been complemented by in-situ hydraulic tests in seafloor drill holes and by fracture maps in ophiolites, in order to capture the combined effects of rock-matrix and fracture permeability (Anderson et al., 1985; Becker and Fisher, 2000; Nehlig, 1994; van Everdingen, 1995). However, little is known about the permeability of basalts that have been hydrothermally altered at temperatures (*T*) up to 450 °C at pressures (*P*) of 30–70 MPa hydrostatic.

At such elevated *P–T* conditions, basalts are transformed into two main assemblages of hydrothermal minerals (Fig. 1). Along deep circulation paths, assemblages of albite + chlorite ± actinolite are stabilized, producing rocks that are termed "spilites" (e.g., Cann, 1969). In contrast, reactions along the upflow path can lead to partial or complete replacement of the spilite assemblage by epidote + quartz, producing

* Corresponding author.
E-mail address: alannah.brett@geo.unibe.ch (A.C. Brett-Adams).
[1] Present address: Institute of Geophysics, Department of Earth Science, ETH Zurich, Switzerland.

https://doi.org/10.1016/j.tecto.2021.228994
Received 31 December 2020; Received in revised form 18 June 2021; Accepted 27 June 2021
Available online 17 July 2021

rocks known as "epidosites" (e.g., Richardson et al., 1987; Gilgen et al., 2016). Rock cores from the deepest drill holes in in-situ oceanic crust typically show only partial alteration to spilite, and epidosites are rare (e.g., Staudigel, 2014). However, basalts altered to end-member spilites and epidosites are common in ophiolites and Archean greenstone belts (Alabaster and Pearce, 1985; Galley et al., 1993; Hannington et al., 2003; Gillis and Banerjee, 2000; Coelho et al., 2015; Gilgen et al., 2016).

The water–rock interaction driving spilite and epidosite alteration has important consequences for mass and heat transfer between the crust and the oceans. These include buffering of the chemical and isotopic composition of seawater (e.g., Mottl and Wheat, 1994; Bach et al., 2003) and leaching of base and precious metals during spilite or epidosite alteration, which may form massive sulfide ore deposits where the hydrothermal fluids discharge at the seafloor (e.g., Hannington, 2014; Jowitt et al., 2012; Patten et al., 2016). Progress in understanding these processes via numerical thermal–hydraulic–chemical modelling would be facilitated by knowing the permeability of the altered rocks along the high *P–T* flow paths.

Samples of basalts that have undergone high temperature alteration are obtainable from drill holes in present-day, cold oceanic crust and from outcrops in ophiolites. Fig. 1 summarizes published rock-matrix permeabilities of fresh and variously altered submarine basalts typical of mid-oceanic ridges and ophiolites, as well as permeabilities modelled for fracture networks and for bulk upper crust permeability based on in-situ hydraulic tests. The ranges of published values demonstrate the heterogeneous nature of permeability in the upper crust and underscore the challenge of estimating realistic crustal-scale values. Moreover, since few experiments on altered basalts at elevated *P–T* conditions have been performed, it is unclear to what extent laboratory and in-situ measurements at low temperature and pressure are valid for the high temperatures and pressures at which the hydrothermal alteration occurred. Subjecting fresh basalts to effective pressures (confining pressure minus pore pressure) up to 50 MPa at room temperature is known to reduce their permeability by up to half an order of magnitude (Christensen and Ramananantoandro, 1988; Fortin et al., 2011; Gilbert and Bona, 2016; Karato, 1983). Experiments on the response of permeability to elevated temperatures have been conducted on fresh submarine basalts (Aksyuk et al., 1992; Shmonov et al., 1995), fresh and weakly altered subaerial andesites (Kushnir et al., 2017). However, comparison of these studies reveals contradictory trends. For the fresh submarine basalts, Aksyuk et al. (1992) found that heating up to 400 °C generally increases permeability, whereas Shmonov et al. (1995) found the opposite. In the subaerial andesites Kushnir et al. (2017) found near-constant permeability up to 600 °C, but in subaerial dacite Gaunt et al. (2016) found that permeability decreases dramatically by 3.5 orders of magnitude upon heating to 500 °C. These differences hinder the recognition of a clear temperature–permeability relationship. To our knowledge, no studies have tested the effect of increasing temperature on the permeability of pervasively altered basalts.

As a step towards filling this gap in knowledge, the present study focuses on how changes in pressure and temperature affect the rock-matrix permeabilities of a small set of spilite and epidosite samples from the Semail and Troodos ophiolites. We first report room temperature experiments carried out over a range of pressures using an unsteady-state gas permeameter. This enables the behavior of the sampled spilites and epidosites under pressure to be compared to that of fresh basalts in previous studies. We then present isobaric permeability experiments at 50 MPa effective pressure over temperatures between 25 and 450 °C using the oscillating flow method in a Paterson gas apparatus (Paterson, 1970). The results allow us to derive empirical correlations between temperature and permeability, which permit standard permeability measurements performed at room temperature and in-situ pressure to be corrected to the in-situ, high *P–T* conditions of hydrothermal circulation in the oceanic crust. Furthermore, the correlations are suitable for use in numerical simulations of hydrothermal flow. Finally, the observed trends and our scanning electron microscope (SEM) observations of samples before and after the experiments provide insights into the mechanisms of the permeability changes.

2. Samples

2.1. Geological setting of sampled spilites and epidosites

Our samples derive from the sheeted dike complexes and comagmatic pillow lavas that formed during the spreading-axis stages of crustal growth in the Semail and Troodos ophiolites (Fig. 1). We have

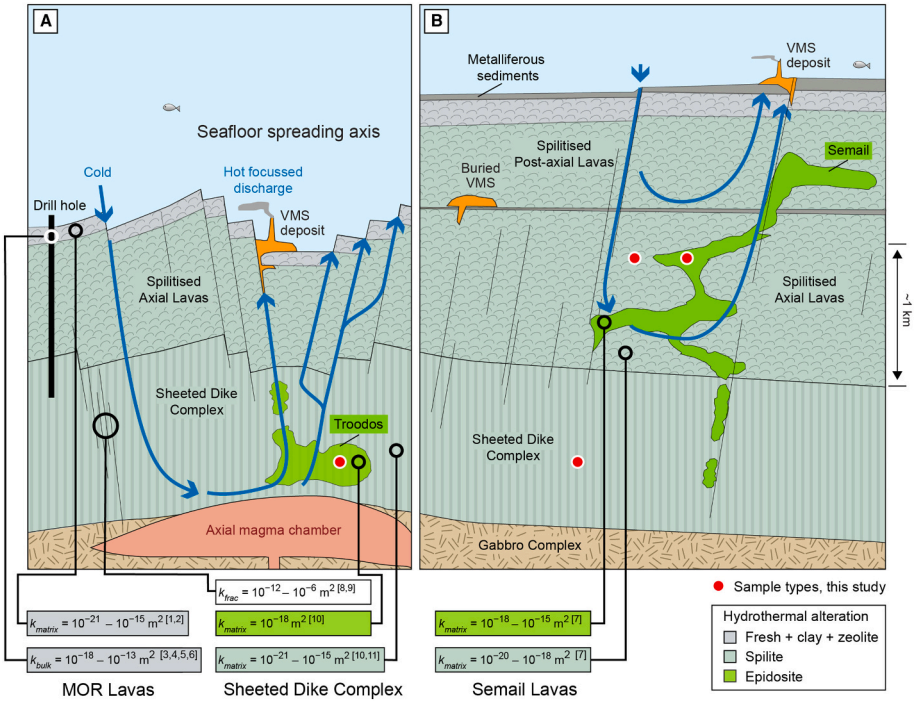

Fig. 1. Schematic cross-sections through the upper oceanic crust based on the Troodos and Semail ophiolites, showing published permeabilities and the distribution of hydrothermal spilite and epidosite alteration, modified from Gilgen et al. (2016). Approximate scale based on Semail ophiolite. (A) Troodos mid-ocean ridge (MOR) volcanic stage with axial Sheeted Dike Complex and comagmatic lavas. Alteration based on Richardson et al. (1987) and Varga et al. (1999); (B) Semail ophiolite post-axial volcanic stage, during which tholeiitic lavas blanket the older axial lavas and comagmatic Sheeted Dike Complex. Alteration based on Alabaster and Pearce (1985) and Gilgen et al. (2016). Published ranges of rock-matrix permeability (k_{matrix}), bulk permeability based on in-situ hydraulic tests (k_{bulk}), and permeability modelled from fracture distributions (k_{frac}) are from [1]Johnson (1980), [2]Jarrard et al. (2003), [3]Anderson et al. (1985), [4]Becker (1989), [5]Becker and Fisher (2000), [6]Fisher (1998), [7]Brett et al. (2017), [8]van Everdingen (1995), [9]Nehlig (1994), [10]Coelho et al. (2015), [11]Gilbert and Bona (2016).

sampled spilites and epidosites from these units to ensure relevance of our results to present-day oceanic crust. However, unlike modern mid-ocean ridge settings, the axial basalts and basaltic andesites in the Semail and Troodos ophiolites are overlain by a 1–2 km thick sequence of off-axis to post-axis primitive basalts, fore-arc tholeiitic lavas and boninitic lavas (Belgrano et al., 2019; Osozawa et al., 2012). Owing to this additional overburden and its thermal insulation effect, the pressures and temperatures of post-axial hydrothermal alteration in the deeper axial lavas and sheeted dikes may have been higher than those attained under present-day mid-ocean ridges. The Troodos lavas are highly altered but volcanic glass is commonly preserved (Gillis and Robinson, 1990). Hydrothermal alteration of the Semail lavas is even stronger and glass is extremely rare (Alabaster and Pearce, 1985; Kusano et al., 2017). At depths greater than the shallow clay and zeolite alteration zones, pervasive spilite alteration is abundant, affecting hundreds of km^2 of lavas and sheeted dikes in both ophiolites (spilitized dikes in Troodos are also termed "diabase"). Fluid inclusion studies have shown that the Semail spilite alteration occurred over a range of *P–T* conditions (160–420 °C and 31–54 MPa hydrostatic; Richter and Diamond, 2019) during both axial spreading and post-axial volcanism. Epidosite alteration is much less abundant than spilite alteration, being limited to distinct zones up to 1 km^2 in outcrop. In the Troodos ophiolite the epidosites are almost exclusively confined to the sheeted dikes (Jowitt et al., 2012) and alteration is thought to have occurred during active oceanic spreading (Varga et al., 1999; Fig. 1A). In the Semail ophiolite the epidosites are dominantly in the overlying lavas, with smaller bodies in the sheeted dikes (Gilgen et al., 2016). Epidosite alteration in the Semail ophiolite post-dated and pervasively replaced spilite altered basalts, and it occurred mostly during post-axial volcanism, regardless of its location in the volcanostratigraphy (Gilgen et al., 2016). Thus, although the sampled Semail lavas and dikes were emplaced and initially altered to spilite during axial-stage volcanism, their hydrothermal overprinting to epidosite occurred after spreading had ceased (Gilgen et al., 2016; Fig. 1B). Fluid inclusions from numerous sites in the volcanostratigraphy constrain the epidosite alteration to 250–440 °C and 35–68 MPa hydrostatic (Richter and Diamond, 2019).

2.2. Sample selection

The locations and lithostratigraphic units of the six samples selected for the experiments are shown in Table 1. In the Semail ophiolite we collected a pillow lava altered to spilite, a pillow lava altered to epidosite and two dikes altered to spilite, all of which originate from different locations in the Geotimes volcanostratigraphic unit (Belgrano et al., 2019) and the co-magmatic sheeted dike complex. As the aim of this study is to define the rock-matrix permeabilities of the spilites and epidosites, care was taken in the field to collect specimens free of macroscopically visible fractures and veins. Two oversized samples were collected where outcrop conditions allowed their extraction by leverage with chisels without heavy hammering, so as to avoid inducing fractures. These samples were subsequently cored in the laboratory. The other two samples from the Semail ophiolite were retrieved as cylindrical plugs using a portable, water-cooled drill equipped with a diamond-tipped core bit of 2.54 cm diameter. In thin-section the collected samples show textures typical of the hundreds of spilite and epidosite thin-sections examined during our regional mapping of the Semail volcanic sequence (Belgrano et al., 2019). From the Troodos ophiolite we obtained a large block of altered basaltic dike showing bands of variable epidosite alteration overprinting spilite alteration. This was collected from the axial sheeted dike complex by Coelho et al. (2015) and used for their Paterson apparatus experiments (their runs PP332 and PP308). This sample is also free of macroscopically visible fractures and veins and it is typical of other samples that we collected for comparison in Troodos.

2.3. Sample mineralogy, textures and porosity

Thin sections of each hand sample used in this study were examined by transmitted-light optical microscopy and by scanning electron microscopy (SEM) in back-scattered electron (BSE) mode before the experiments and a selection of the samples were examined after the experiments.

None of the samples contain glass. They are either composed entirely of hydrothermal minerals or of a combination of hydrothermal minerals and relict igneous minerals from the original fresh basalts. All the rock textures (Fig. 2) are isotropic at the cm^3 scale.

The spilite lava and dike samples (LD10-104-3; AB17-32C-spl and SG14-43) contain hydrothermal albite, chlorite, actinolite, quartz, titanite and hematite, plus relict igneous clinopyroxene and titanomagnetite. Three types of pores are present: (1) Interstitial pores (< 10 μm diameter in the lava; < 50 μm diameter in the more coarsely crystalline dike) arrayed along the crystal boundaries (Fig. 2A–C), including characteristic swarms of micropores (< 1 μm diameter) between the very fine crystallites that make up the chlorite aggregates (observable only at high magnification in SEM); (2) Volcanic vesicles (< 300 μm diameter) are present in the lavas but they contribute little to overall porosity, as they are mostly filled by chlorite, epidote or quartz; (3) Rare microfractures and veinlets (≤ 1 mm length; < 10 μm aperture) that crosscut the crystal matrix along meandering and branching paths. The fractures have parallel but undulating, irregular walls, showing that

Table 1
Samples used in this study, including porosity and unsteady-state permeameter measurements at 25 °C.

Sample name	Ophiolite	Lithostrati-graphic unit	Location (UTM zone; coordinates mN, mE)	Rock type[a]	He-accessible porosity (vol%)	Permeability[b] at 25 °C and P_e = 50 MPa[c] (m^2)
CO-51-e[d]	Troodos	Dike complex	36 N; 496,904 3,869,828	Partial-epidosite dike	10.0	1.60×10^{-16}
CO-51-s[d]	Troodos	Dike complex	36 N; 496,904 3,869,828	Partial-epidosite dike	6.0	3.36×10^{-18}
SG14-56	Semail	Geotimes lavas	40 N; 431,785 2,739,627	Epidosite pillow lava	4.1	9.85×10^{-17}
AB17-32C-spl	Semail	Geotimes dike complex	40 N; 538,351 2,608,870	Spilite dike	4.8	2.46×10^{-19}
LD10-104-3	Semail	Geotimes lavas	40 N; 468,748 2,656,024	Spilite pillow lava	5.1	5.56×10^{-19}
SG14-43[e]	Semail	Geotimes dike complex	40 N; 431,747 2,739,254	Spilite dike	0.57	Below detection

[a] Glass-free hydrothermally altered basalts (see Supplementary Material for chemical compositions of samples).
[b] Measured by unsteady-state gas permeameter on 25 mm diameter cylindrical cores. Note that the high–*T* experiments (Table 2) were performed on smaller cores.
[c] P_e is the effective pressure = confining pressure minus pore pressure.
[d] Samples drilled from the same hand-specimen used in experiments by Coelho et al. (2015; their runs PP332 and PP308).
[e] Spilite dike sample from which the two adjacent and homogeneous plugs SG14-43-1 and SG14-43-2 were used for compression experiments, average porosity of the two plugs provided, permeability value available for 5 MPa in Table 3.

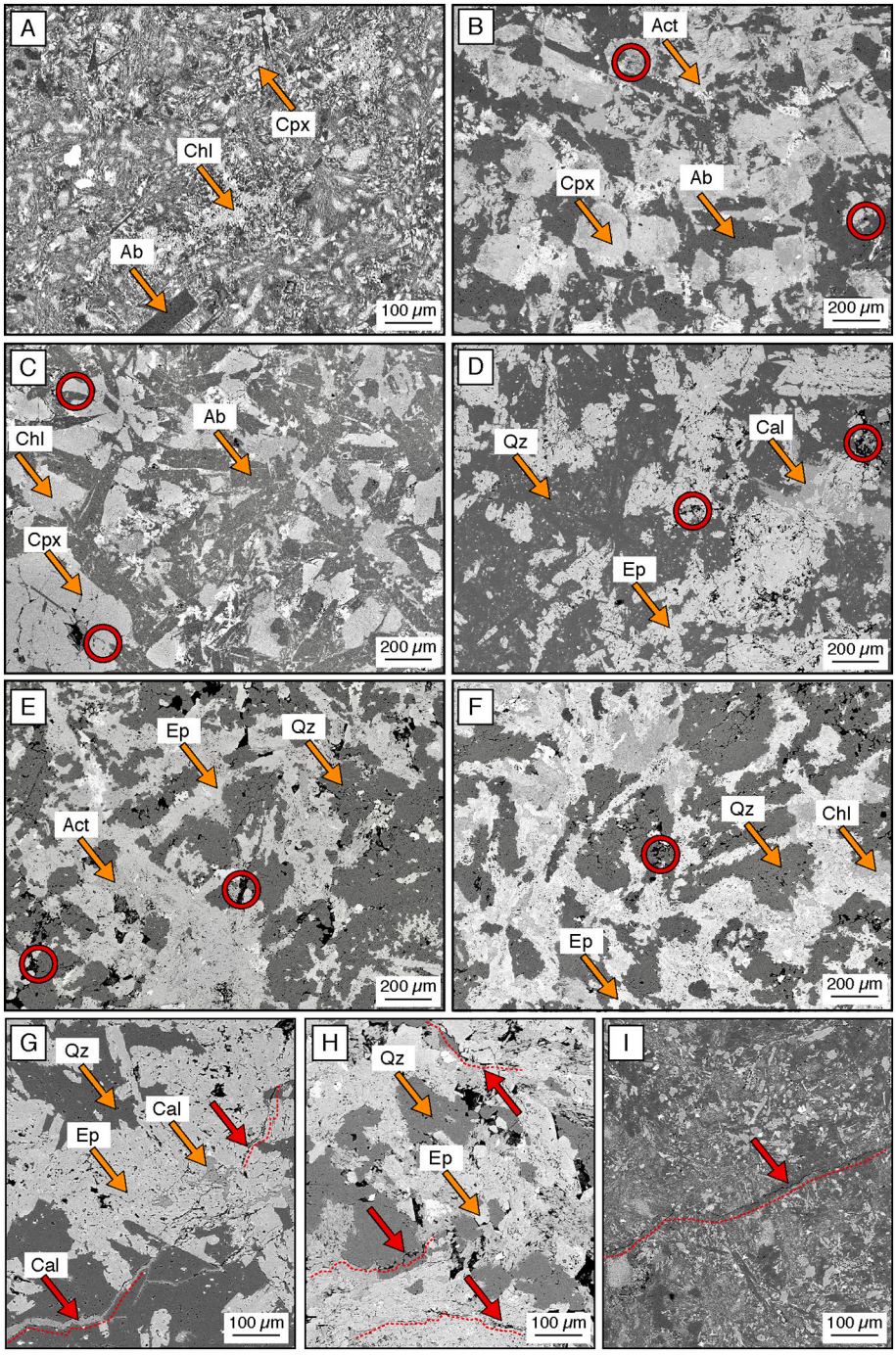

Fig. 2. Images in SEM–BSE mode of the six samples used in this study including examples of pre-existing microfractures prior to the experiments. Pores appear black (examples marked by red circles); microfracture are open (black) and/or filled by hydrothermal minerals (both marked by red arrows and dotted lines). Abbreviations: Chl – chlorite, Ab – albite, Cpx – clinopyroxene, Ep – epidote, Qz – quartz, Act – actinolite, Cal – calcite. (A) Spilitized pillow lava LD10-104-3. (B) Spilitized dike AB17-32-spl. (C) Spilite dike SG14-43. (D) Epidotized pillow lava SG14-56. (E) Partially epidotized dike CO-51e. (F) Partially epidotized dike CO-51 s, a duplicate from the same hand sample as for (D). (G) Short microfractures partly filled by calcite in epidotized pillow lava SG14-56. (H) Short open microfractures in partially epidotized dike CO-51 s. (I) Long microfracture that crosscuts the maxtrix, partly open and partly quartz-filled in spilitized pillow lava LD10-104-3. (For interpretation of the references to colour in this figure legend, the reader is referred to the web version of this article.)

they formed by simple extension without any signs of shear displacement. Typically some segments of individual fractures are open and some segments are sealed by quartz or calcite (e.g. Fig. 2I). The porosities of the spilites determined by He-pycnometry are ~5.1 vol% for the pillow lava and ~0.6–4.8 vol% for the dikes (Table 1). These values lie within the measured ranges of ~3–5 vol% in spilite lavas from the Semail ophiolite (Christensen and Smewing, 1981) and ~0.5–5.5 vol% in spilite dikes from IODP Hole 1256 (Gilbert and Salisbury, 2011; Violay et al., 2010) and DSDP Hole 505B (Pezard, 1990).

The epidotized pillow lava and dike samples are dominated by zones of granoblastic, interlocking epidote and quartz, with accessory titanite and hematite or magnetite. Significant amounts of relict actinolite and chlorite are preserved in the epidosites from the precursor spilites and so the epidosites used in this study are in fact partial epidosites rather than end-members. For convenience herein we refer to these samples simply as "epidosites". The pore types in the epidosite zones of the samples are: (1) interstitial pores of 50–200 μm in diameter (Fig. 2D–F), notably larger than in the spilites; (2) microfractures with the same dimensions as the rare microfractures in the spilites, partly filled with epidosite-age quartz and post-epidosite calcite. Such microfractures are rare in the dike samples CO-51e and CO-51 s (e.g. Fig. 2H) but are common in the epidosite lava SG14-56 (Fig. 2G). Very small amounts of calcite clog a few pores in sample SG14-56 (Fig. 2D,G). This calcite is petrographically younger than and hence unrelated to the spilite and epidosite alteration of interest (Belgrano et al., 2019). The porosities of the epidosites determined by He-pycnometry are 4.1 vol% for the pillow lava and 6–10 vol% for the dikes (Table 1). Because these samples are only partial epidosites, their porosities are lower than the ~13 vol% typical of end-

member epidosites (Brett et al., 2017).

3. Experimental methods

3.1. Selection of experimental conditions

Two series of permeability experiments were performed: the first during isothermal compression of the samples at room temperature (blue symbols in Fig. 3), and the second during isobaric heating and cooling cycles (red symbols in Fig. 3). The hydrostatic pressure during spilite and epidosite alteration in the Semail ophiolite is estimated to have been between 31 and 68 MPa (Richter and Diamond, 2019), and the epidosite alteration at Troodos likely occurred near 40 MPa (Richardson et al., 1987). To cover most of this range we performed our isothermal compression experiments at effective pressures between 5 MPa and 55 MPa at 25 °C. The isobaric heating–cooling series was performed at 50 MPa effective pressure, achieved by applying a confining pressure of 100 MPa and a pore pressure of 50 MPa. As well as corresponding to the average of the hydrostatic pressure estimates for the Semail alteration, the chosen 50 MPa pressure matches the value widely used in experimental studies to represent hydrothermal alteration in mid-ocean ridge systems in general (e.g., Seyfried et al., 1988; Coelho et al., 2015).

The primary temperature interval of interest for the isobaric cooling–heating experiments is given by the 160–440 °C range at which the Semail and Troodos samples underwent hydrothermal alteration (Coelho et al., 2015; Richardson et al., 1987; Richter and Diamond, 2019). A practical requirement of our high-*T* apparatus is that the sample must first be briefly heated to 500 °C to seal a copper jacket around the sample before commencing permeability measurements.

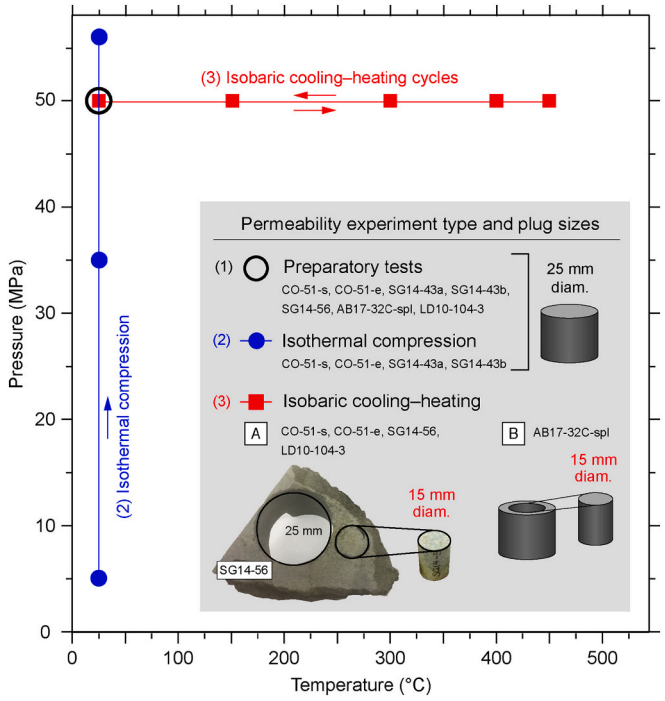

Fig. 3. Pressure–temperature diagram showing the three kinds of experiments in this study and the sample sizes used: (1) preparatory permeability tests at room temperature and 50 MPa effective pressure (data in Table 1); (2) isothermal compression at room temperature and 5, 35 and 55 MPa effective pressure (data in Table 3); (3) isobaric cooling–heating at 50 MPa effective pressure and temperatures of 25, 150, 300, 400 and 450 °C (data in Table 4). (A) Example of the four samples from which a 15 mm diameter mini-plug was cored next to a 25 mm diameter plug. (B) The sample in which a 15 mm mini-plug was cored from within a 25 mm plug.

This elevated temperature is still within the stability field of the minerals in the samples, as confirmed by our thermodynamic calculations using the data in Holland and Powell (2011). Accordingly, no mineralogical changes are expected during the relatively short-term, nominally water-free experiments, although chlorite is prone to liberate water (discussed further below). Another experimental requirement was to end our high-*T* experiments with measurements at room temperature, in order to facilitate comparison of the results with the isothermal compression measurements. Our isobaric permeability measurements were therefore made at discrete steps between 25 and 400 or 450 °C (Fig. 2).

3.2. Preparatory measurements

Plugs of 25 mm diameter and 20–30 mm length were drilled from all the hand specimens (e.g., Fig. 3A) and their ends were trimmed by a slowly turning diamond saw to produce perfect right-angle circular cylinders. Their gas-accessible porosity was measured in our laboratory in Bern using a helium pycnometer (Micromeritics™ AccuPyc II 1340), and their permeability at 25 °C and 50 MPa effective pressure was measured in a CMS™-300 unsteady-state, pressure-decay permeameter using helium as the pore fluid (e.g. Honarpour et al., 1986) at CoreLab, Aberdeen. The uncertainty of the permeability measurements is ~10%, the detection limit is $\sim 9.8 \times 10^{-20}$ m^2, and all results were corrected for the *P*–*T* dependency of helium viscosity and for the Klinkenberg effect. The results are listed in Table 1.

The above preparatory measurements helped determine which samples were suitable for experiments at high temperatures, as the employed oscillating flow method (described in Section 3.4.1) can measure only a limited range of permeabilities. Two high-temperature scoping experiments on altered basalts with room-temperature permeabilities of $\sim 1 \times 10^{-19}$ m^2 and $\sim 4 \times 10^{-15}$ m^2 showed that these samples are too impermeable and too permeable, respectively, to be accurately measured by the oscillating flow method. Therefore, for further experiments, samples were selected from within this permeability range.

3.3. Permeability measurements upon isothermal compression

In order to quantify the effect of isothermal compression on permeability, four 25 mm diameter plugs from two samples (Fig. 3) were measured at 25 °C in the unsteady-state permeameter described above, with the same uncertainties, detection limit and Klinkenberg correction. Pore fluid pressure was maintained at ~0.2 MPa and measurements were made at effective pressures of ~5, 34 and 55 MPa by increasing the confining pressure. The individual measurements were made after a 7–8 min equilibration time.

3.4. Permeability measurements at elevated pressure and temperature

3.4.1. Principle of the oscillating flow method

An internally heated, Paterson triaxial gas apparatus (Paterson, 1970) at ETH-Zurich was used to measure the permeability of cylindrical rock plugs by the oscillating flow method (Bernabé et al., 2006; Fischer, 1992; Kranz et al., 1990) at various temperatures under constant confining and pore pressures. During the experiments the cylindrical surface of the sample plug is sealed by a malleable copper jacket. Meanwhile, the ends of the plug are open to upstream and downstream argon gas reservoirs at the selected pore pressure. A computer-controlled pump induces sinusoidal pressure oscillations of ~2 MPa amplitude in the upstream gas reservoir, which traverse the sample and are detected in the downstream reservoir. Owing to the rock sample characteristics, to the gas properties and to the characteristics of the experimental setup, the pressure oscillations in the downstream reservoir show an attenuated amplitude and a phase shift. The amplitude ratio and phase shift of the recorded signals are then employed to calculate the permeability of the sample by solving the following

equation (Bernabé et al., 2006):

$$Ae^{i\theta} = \left(\frac{1+i}{\sqrt{\xi\eta}}sinh\left[(1+i)\sqrt{\frac{\xi}{\eta}}\right] + cosh\left[(1+i)\sqrt{\frac{\xi}{\eta}}\right]\right)^{-1} \quad (1)$$

where A is the amplitude ratio, θ the phase shift, and η and ξ the non-dimensional permeability and storativity as follows:

$$\eta = \frac{S\tau k}{\pi L \mu \beta_D} \quad (2)$$

and

$$\xi = \frac{SL\beta}{\beta_D} \quad (3)$$

where S is the sample cross-sectional area, L the sample length, μ the P–T dependent fluid viscosity, τ the time period, β_D the downstream storage capacity, β the sample storativity, and k the sample permeability. A detailed discussion of the associated calculations, limitations and uncertainties of the oscillating flow method are given by Kranz et al. (1990) and Bernabé et al. (2006).

3.4.2. Sample preparation and experimental assembly

As the apparatus requires cylindrical samples of 15 mm diameter and 15–20 mm length, new mini-plugs were prepared as illustrated in Fig. 3. Sample AB17-32-spl was drilled from the 25 mm diameter plug previously measured for porosity and permeability at room temperature (Fig. 3B). In the case of the other four samples, the original 25 mm diameter plugs had been damaged or milled for geochemical analysis and so new mini-plugs were drilled from the original hand-specimen directly adjacent to the 25 mm drill hole (Fig. 3A). The mini-plugs were precision-ground at both ends on a lathe under running water, then dried in an oven at 60 °C for at least 48 h.

For each experiment a mini-plug was placed into the sample column between zirconia and alumina pistons, which each contain a central 2 mm hole to permit the flow of argon. Even distribution of the gas at the upstream and downstream ends of the sample was facilitated by a cross groove in each of the alumina spacers in contact with the sample. A copper jacket of 15 mm inner diameter and 0.2 mm thickness was fitted snugly around the sample to isolate the pore-fluid gas from the gas used to transmit the confining pressure. The sample column was then inserted into a furnace and the furnace lowered into a pressure cell. Finally, the pressure cell was closed, and anodes were attached to control the furnace temperature, along with a thermocouple to monitor the temperature directly above the sample.

3.4.3. Permeability measurements

After sample loading, both the confining and pore pressure systems were flushed five times with argon to saturate them and to clear any residual air. The confining pressure (P_c) was first increased to 100 MPa and then the pore pressure (P_p) was raised to 50 MPa. The copper jacket was sealed around the sample by increasing the temperature from 25 to 500 °C over ~1 h and maintaining this temperature for 15 min. The first experimental run was then executed by allowing the sample to cool for isothermal measurements at 450 °C, 400 °C, 300 °C, 150 °C and 25 °C, while maintaining P_c at 100 MPa via a gas intensifier. The heating and cooling rates were at most 10 °C/min, with lower rates set automatically by the heating controller to avoid overshooting as the target temperature was approached. Prior to each measurement, the temperature was held constant for 10 min to equilibrate the desired temperature across the 15 mm diameter sample. This equilibration time was demonstrated to be sufficient by prior furnace tests made to calibrate the sample temperature and also by the excellent reproducibility of the permeability measurements (within experimental uncertainties) between cooling and heating runs (Fig. A1).

At the start of each experiment, test oscillations were induced to optimize the attenuated amplitude and phase offset within the limits required for best accuracy, as recommended by Bernabé et al. (2006 and references therein). The optimal settings for each sample are listed in Table 2. Thereafter at each temperature step, twenty-five pressure oscillations were recorded in the downstream reservoir, entailing 27–60 min of measurement time.

In addition to the initial cooling runs, measurements were repeated on three samples at the same temperature and pressure conditions during subsequent heating and cooling runs. These runs were carried out to test for reproducibility and for any hystereses dependent on the direction of temperature change. The spilitized pillow and dike samples required several days for these measurements owing to their low permeability. During the 2–3 days between each run the sample was held for safety reasons at room temperature and P_c was decreased to ~30 MPa and P_p to 5 MPa. Once the elevated pressures were restored after these breaks, measurements were carried out at 25 °C and then during heating at 150 °C, 300 °C and 400 °C. Additional measurements on the spilite dike were made at 300 °C, 150 °C and 25 °C during a second cooling run on the same day. Similarly, the high permeability of the epidosite pillow sample required only short measurement times (Table 2). Thus, its initial cooling run was followed by a heating run to 400 °C on the same day, yielding seven measurements. After the 2–3 day pause, a second run of heating and cooling measurements was performed, totaling 14 measurements for this sample.

3.4.4. Calculation of permeability

Of the 25 oscillations recorded at each temperature step, the first six were discarded to avoid any early transient effects on the recorded downstream signal (Bernabé et al., 2006). Ten cycles were then used for the permeability calculation. The oscillation data were processed with the a MATLAB™ code that solves Eq. (1) numerically for permeability and storativity by applying an iterative gradient-based optimization method with adaptive step size to improve convergence of the solution. Due to the high downstream reservoir storage of the employed pump, the storativity may attain unrealistic negative values and was therefore not considered in our measurements (Bernabé et al., 2006). The viscosity of argon in Eq. (2) was adjusted for each P–T point of measurement according to the equation of state of Tegeler and Wagner (1999). Following Faulkner and Rutter (2000), no Klinkenberg correction for gas slippage was applied because our calculations using the Van der Waals radius of 188 pm for argon showed that the mean free path of argon atoms is < 0.31 nm under the high effective pressure (50 MPa) at all experimental temperatures (20–450 °C). Based on our SEM observations, this is considerably smaller than the likely diameter of pore throats in our samples.

3.4.5. Examination of microstructures after isobaric cooling–heating experiments

Thin sections were made from three of the mini-plugs used for the high temperature permeability experiments (CO-51 s, LD10-104-3 and SG14-56; Table 1). A low speed diamond-coated wire saw was used to cut each plug at two orientations: (1) across the plug perpendicular to its long axis, resulting in a circular section, and (2) along the length of the plug parallel to its long axis, resulting in a rectangular section. The sections were prepared with a standard single-side polish and 30 μm thickness. Imaging by SEM-BSE was used to check for microfractures or textural features caused by the high temperature experiments.

4. Results

4.1. Effect of elevated pressure on the permeability of spilites and epidosites

Applying increasing effective pressure to the samples at room temperature in the gas permeameter decreased the permeability of the two cores from the spilitized dike (SG14-43-1 and SG14-43-2) and the two

Table 2
Sample dimensions and pressure oscillation parameters used in high temperature experiments.

Sample	Core diameter[a] (mm)	Core length (mm)	Pressure pulse amplitude (MPa)	Pressure pulse frequency (Hz)	Amplitude ratio[b]	Phase offset (cycles)	Time for 25 oscillations (min)
CO-51-e	15	20.01	2	0.010	0.27	0.21	40
CO-51-s	15	19.00	2	0.010	0.25	0.24	40
SG14-56	15	20.00	2	0.015	0.20	0.23	27
AB17-32C-spl	15	16.04	2	0.009	0.08	0.31	46
LD10-104-3	15	17.25	2	0.007	0.04	0.35	59

[a] Note that these cores are smaller than those used for the gas permeameter measurements at 25 °C (Table 1).
[b] Downstream/upstream pressure ratio.

cores from the epidotized dike (Co-51-e and Co-51-s; Fig. 4 and Table 3). Between 5 and 55 MPa effective pressure the permeability of the epidosites decreased by absolute values of 7.3×10^{-17} m^2 (31% relative decrease; Co-51-e) and 7.2×10^{-18} m^2 (68%, CO-51-s). The spilitized dike samples showed larger relative decreases in permeability between 5 and 33 MPa of at least 4.0×10^{-19} m^2 (80% relative decrease; SG14-43-1) and 9.9×10^{-20} m^2 (50%; SG14-43-2). The experimental detection limit at 9.8×10^{-20} m^2 (labelled LOD in Fig. 4) was reached at 33 MPa, therefore the quoted decreases in absolute and relative permeabilities of the two spilite samples are minimum values.

4.2. Experiments at elevated temperatures

4.2.1. Effect of elevated temperature on the permeability of spilites and epidosites

During the initial cooling runs in the oscillating flow experiment, the permeability of each sample increased from the initial measurement at either 450 or 400 °C to the final measurement at 25 °C, thereby defining a systematic trend of increasing permeability with decreasing

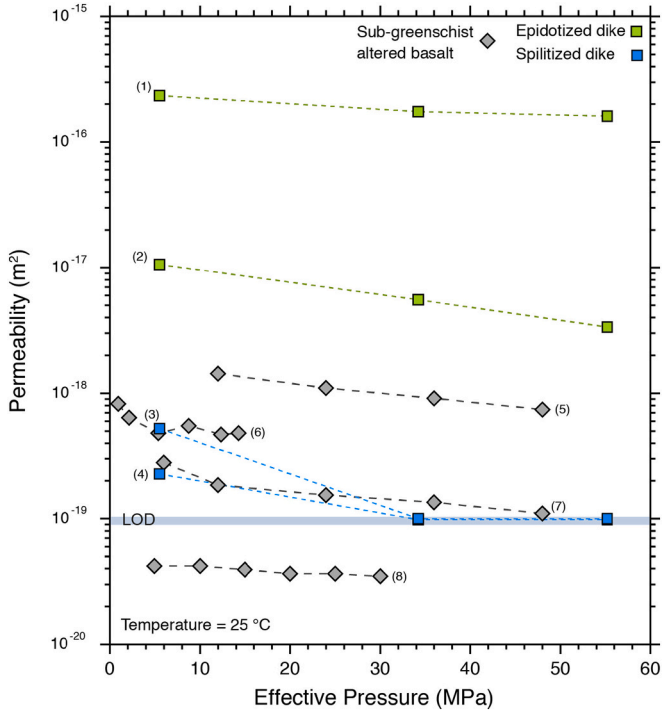

Fig. 4. Permeability measured by standard permeameter as a function of effective pressure at 25 °C. (1), (2) dikes altered to epidosite (green, this study). (3), (4) dikes altered to spilite (blue, this study; LOD denotes limit of detection for our study). Literature data from basalts altered at sub-greenschist conditions: (5), (7) Christensen and Ramananantoandro (1988), (6) Karato (1983), (8) Gilbert and Bona (2016). (For interpretation of the references to colour in this figure legend, the reader is referred to the web version of this article.)

Table 3
Permeabilities of 25 mm diameter cores of spilitized and epidotized dikes over a range of effective pressures at 20 °C.

Sample	Sample type[a]	Confining pressure (MPa)	Mean pore pressure (MPa)	Effective pressure (MPa)	Permeability[b] (m^2)
SG14-43-1	Spilitized dike	5.5	0.25	5.3	4.93×10^{-19}
SG14-43-1		33.5	0.25	33.3	Below detection
SG14-43-1		55.2	0.25	54.9	Below detection
SG14-43-2	Spilitized dike	5.5	0.26	5.2	1.97×10^{-19}
SG14-43-2		33.5	0.26	33.2	Below detection
SG14-43-2		55.2	0.26	54.9	Below detection
CO-51-e	Partial-epidosite dike	5.5	0.17	5.3	2.34×10^{-16}
CO-51-e		33.5	0.17	33.3	1.74×10^{-16}
CO-51-e		55.2	0.17	55.0	1.60×10^{-16}
CO-51-s	Partial-epidosite dike	5.5	0.20	5.3	1.06×10^{-17}
CO-51-s		33.5	0.20	33.3	5.53×10^{-18}
CO-51-s		55.2	0.20	54.9	3.36×10^{-18}

[a] See Supplementary Material for chemical compositions of samples.
[b] Klinkenberg-corrected values and detection limit of ~9.8×10^{-20} m^2.

temperature (Fig. 5; Table 4). The only exception to this trend was a near constant permeability (within error) recorded for the spilite dike and spilite pillow samples at 400 °C and 300 °C, after which the permeability followed the trend of the other samples.

In the epidosite dikes, permeabilities increased upon cooling from 450 °C to 25 °C by absolute values of 2.2×10^{-18} m^2 (47% relative increase) and 2.4×10^{-18} m^2 (50%), and similarly the permeability of the epidosite pillow lavas increased by 1.9×10^{-18} m^2 (44%). Over the same cooling range the permeabilities of the spilite dike and spilite pillow samples increased by 1.8×10^{-19} m^2 (38%) and 1.27×10^{-19} m^2 (36%), respectively.

The dike samples show lower permeabilities at 25 °C than those measured in the isothermal compression experiments (cf. Figs. 4 and 5). The reason for this difference is that different parts of the same samples were measured in the two different experiments, as shown in Fig. 3. These results demonstrate that the epidosite and spilite dikes have markedly heterogeneous permeabilities at the cm-scale.

4.2.2. Production of water during experiments

Upon disassembling the two experiments on the epidotized dike (Co-51-e and Co-51-s), a thin film of water was found between the alumina spacer and the top of the sample. The samples themselves appeared

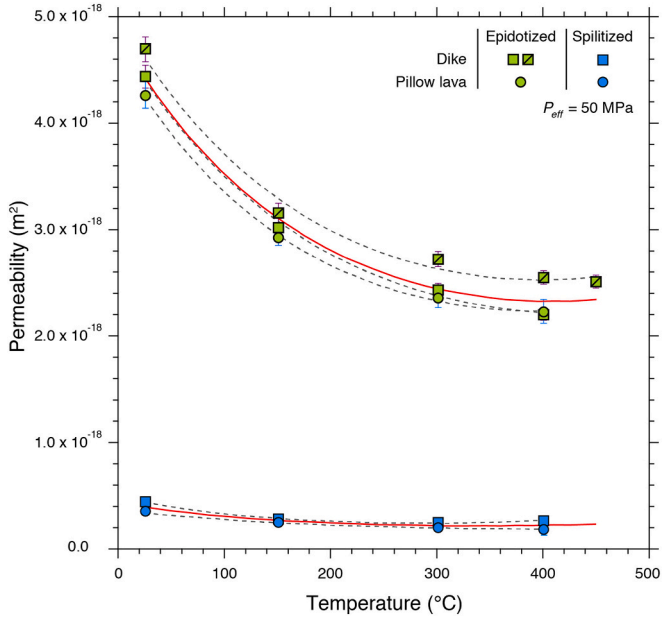

Fig. 5. Measured permeability of spilitized and epidotized pillow lavas and dikes at 50 MPa effective pressure. Note that the *y*-axis scale is linear. Data for the epidotised dikes are from initial cooling runs, with analytical uncertainties shown by purple error bars. Data for the spilites and the epidotised pillow lava are mean values from repeated heating and cooling cycles, with ±1 standard deviation shown by blue error bars where deviations are larger than the data symbols. See Table 4 for all data. Red curves show fits for each alteration type according to Eqs. (4) and (5) in the text. (For interpretation of the references to colour in this figure legend, the reader is referred to the web version of this article.)

slightly darker and grayer after the experiments but without any reddish tinge. No water was found in the other experiments.

4.3. Behavior and uncertainty of permeability over multiple cooling and heating cycles

The results of repeated heating and cooling experiments on the epidosite pillow, spilite dike and spilite pillow samples are shown in Table 4 and Fig. A1. The repeats exhibit the same trend as that observed in the initial cooling runs. However, the absolute values of the permeabilities shifted very slightly between runs. Based on the data in Table 4 the means of the repeat measurements and their associated standard deviations were calculated for the two spilites and the epidotised pillow lava and plotted in Fig. 5. These standard deviations for individual samples are comparable to the analytical uncertainty calculated for individual measurements (Table 4), and they have values 2–3 orders of magnitude lower than the measured permeabilities. Overall, the measurements of all samples of each alteration type at any given temperature is reproducible to within 17.5% in the epidosites and 35% in the spilites.

4.4. Temperature–permeability correlations

The temperature–permeability data for individual samples describe smooth logarithmic trends that are well fitted by second-order polynomial functions of the $\log_{10}(k)$ values (gray dashed curves in Fig. 5). Because the differences between the samples of each alteration type are small and their fitted curves are subparallel, we present a mean correlation for each alteration type (red curves in Fig. 5), corresponding to the following for epidosites:

$$log(k) = -18.3169–0.00156T + 1.9155 \times 10^{-6}T^2 \quad (4)$$

and the following for spilites:

$$log(k) = -18.2615–0.00177T + 2.6251 \times 10^{-6}T^2 \quad (5)$$

where k is permeability (m^2) and T is temperature between 0 and 450 °C.

4.5. Petrographic observations following high-temperature experiments

Transmitted-light microscopy of thin sections made of the samples after the experiments showed no changes in optical properties of the minerals, including chlorite. Fig. 6. shows SEM-BSE images of thin sections made from three of the five mini-plugs used in the high temperature experiments. No signs of irreversible deformation are present around interstitial pores or vesicles. Pre-existing microfractures that crosscut crystal boundaries and that are partly filled by hydrothermal calcite or quartz are visible in the sections (Fig. 6A, B), identical to those in the samples prior to the experiments (Fig. 2G–I). There are no indications, such as cracking of the quartz and calcite fillings, that these microfractures expanded irreversibly during the experiments, and there is no evidence that new microfractures formed. The timing of the microfracture in sample CO-51 s is ambiguous (Fig. 6C): it appears identical to segments of pre-existing fractures that show no quartz or calcite fillings (cf. Fig. 6A), but it could also have formed during the experiments or during thin-section preparation.

5. Discussion

5.1. Effects of pressure on permeability

The mostly gradual reduction of permeability with increasing pressure shown by our spilite and epidosite samples (Fig. 4) is presumably due in part to restriction of throats between interstitial pores upon elastic compression. The main effect of compression is probably closure of microfractures (e.g. Fig. 2G–I), as previously demonstrated by studies of permeability, P- and S-wave velocities and acoustic emissions on fresh, glassy basalt (e.g., Fortin et al., 2011; and Nara et al., 2011).

Trends similar to our samples were found in previous studies on fresh glassy basalts and on basalts altered at low temperatures to glass, clays and zeolites (Fig. 4; Christensen and Ramananantoandro, 1988; Karato, 1983; and Gilbert and Bona, 2016). The datasets in Fig. 4 show markedly different absolute permeabilities and minor differences in pressure–permeability slopes, which are attributable to differences in sample mineralogy and texture. The data of Gilbert and Bona (2016) follow the same pressure–permeability trend as the other studies even though the measurements were made on brine-saturated samples rather than using dry gas as the pressure medium, which could have resulted in mineral reactions. Only the results of Karato (1983a) show a sharp kink with increasing pressure below 5 MPa. This may be a real property of the samples or an artifact due to initially incomplete sealing of the sample jacket. All the other studies used a minimum confining pressure of 5 MPa to ensure a good seal.

5.2. Effects of temperature on permeability

5.2.1. Systematic changes in permeability with temperature

Accepting that the measured temperatures, pressures and permeabilities in the oscillating flow experiments are accurate, the repeated heating and cooling experiments demonstrate that the thermally induced changes in permeability of both the spilites and the epidosites are essentially reversible (Fig. A1). The absence of systematic hystereses implies that the mean permeabilities of individual samples (± 9% in epidosites and ± 17.5% in spilites) at each *P*–*T* point represent values at thermomechanical equilibrium, i.e., the values are independent of the rate and direction of temperature change.

The crystalline matrices of our samples undoubtedly expanded upon isobaric heating in our non-isochoric Paterson apparatus, as dictated by

Table 4
Permeabilities of spilites and epidosites measured at elevated temperatures at 50 MPa effective pressure in initial cooling runs and following heating and cooling runs.

Sample and sample type	Run type	Run day	Temperature[a] (°C)	Permeability (m^2)	Analytical uncertainty[b] (m^2)	Δk[c] (%)
CO-51-e Partial-epidosite dike	Cooling	Day 1	450	2.51×10^{-18}	6.11×10^{-20}	–
			400	2.55×10^{-18}	6.31×10^{-20}	1.6
			300	2.73×10^{-18}	7.18×10^{-20}	12
			150	3.16×10^{-18}	8.82×10^{-20}	19
			26	4.69×10^{-18}	1.16×10^{-19}	24
CO-51-s Partial-epidosite dike	Cooling	Day 1	400	2.20×10^{-18}	5.45×10^{-20}	–
			300	2.43×10^{-18}	6.40×10^{-20}	15
			150	3.03×10^{-18}	8.45×10^{-20}	24
			26	4.44×10^{-18}	1.09×10^{-19}	23
SG14-56 Epidosite pillow lava	Cooling	Day 1	400	2.34×10^{-18}	5.81×10^{-20}	–
			300	2.48×10^{-18}	6.54×10^{-20}	11
			150	2.88×10^{-18}	8.03×10^{-20}	19
			26	4.19×10^{-18}	1.03×10^{-20}	22
	Heating	Day 1	150	2.96×10^{-18}	8.27×10^{-20}	−25
			300	2.37×10^{-18}	6.24×10^{-20}	−33
			400	2.21×10^{-18}	5.48×10^{-20}	−14
	Heating	Day 2	26	4.40×10^{-18}	1.09×10^{-19}	–
			150	3.01×10^{-18}	8.40×10^{-20}	−29
			300	2.30×10^{-18}	6.06×10^{-20}	−39
			400	2.12×10^{-18}	5.26×10^{-20}	−15
	Cooling	Day 2	300	2.27×10^{-18}	5.98×10^{-20}	12
			150	2.85×10^{-18}	7.80×10^{-20}	25
			26	4.18×10^{-18}	1.03×10^{-19}	23
AB17-32C-spl Spilite dike	Cooling	Day 1	400	2.19×10^{-19}	7.21×10^{-21}	–
			300	2.77×10^{-19}	7.31×10^{-21}	1
			150	3.07×10^{-19}	8.57×10^{-21}	15
			26	4.66×10^{-19}	1.15×10^{-20}	26
	Heating	Day 2	26	4.50×10^{-19}	1.11×10^{-20}	–
			150	2.66×10^{-19}	7.43×10^{-21}	−49
			300	2.32×10^{-19}	6.12×10^{-21}	−21
			400	2.40×10^{-19}	5.95×10^{-21}	−3
	Cooling	Day 2	300	2.36×10^{-19}	6.22×10^{-21}	4
			150	2.72×10^{-19}	7.60×10^{-21}	18
			26	4.11×10^{-19}	1.01×10^{-20}	25
LD10-104-3 Spilite pillow lava	Cooling	Day 1	400	2.24×10^{-19}	5.54×10^{-21}	–
			300	2.17×10^{-19}	5.71×10^{-21}	3
			150	2.62×10^{-19}	7.32×10^{-21}	22
			26	3.50×10^{-19}	8.64×10^{-21}	15
	Heating	Day 2	26	3.61×10^{-19}	8.90×10^{-21}	–
			150	2.39×10^{-19}	6.68×10^{-21}	−33
			300	1.87×10^{-19}	4.93×10^{-21}	−36
			400	1.46×10^{-19}	3.61×10^{-21}	−37

[a] From top to bottom in order of measurement.
[b] Permeability uncertainty resulting from measurements and experimental parameters inaccuracies.
[c] Relative permeability change with respect to previous temperature step ($k_{step\ 2} - k_{step1}$) / k_{step1}.

the weighted sum of the thermodynamic expansivities of the constituent minerals. The coefficients of compression and thermal expansion given in the thermodynamic database of Holland and Powell (2011) show that the epidosites steadily expanded by 1.20 vol% between room temperature and 450 °C at 50 MPa effective pressure, and that the spilites expanded by 1.19 vol% over the same interval. Furthermore, no irreversible deformation occurred around any of the pores in the samples. If the rock matrix behaves as a coherent interlocked aggregate, its bulk isotropic thermoelastic expansion during heating will cause the confined interstitial pores and very short microfractures (<~200 μm length; e.g. Fig. 6B) to expand by the same relative amounts as the surrounding matrix. As this simple process cannot explain systematic reduction in permeability exhibited by our samples (Fig. A1), other processes need to be considered, as discussed in the following.

5.2.2. *Thermally induced processes that reduce permeability*

Experiments on a wide range of rock types have revealed both positive and negative correlations between permeability and temperature (Bakker et al., 2015; Guo et al., 2017; Liu et al., 2018; Nahhas et al., 2019; Kozusnikova and Konečný, 2011; Kushnir et al., 2017; Shmonov et al., 1995; Sun et al., 2016; Zaraisky and Balashov, 1995). Several of these studies have suggested mechanisms for the reduction of permeability with temperature increase. Regarding experiments in water at elevated temperatures, it has been proposed that permeability can be reduced by crack-sealing due to mineral precipitation (Kushnir et al., 2017) or by pressure solution closing grain boundaries (e.g., in granites: Zaraisky and Balashov, 1995). Such effects are not expected in our experiments because we used a non-reactive gas rather than water and because the hydrothermal minerals in our samples are thermodynamically stable at the imposed pressures and temperatures (Section 3.1).

Despite having used a water-free experimental setup, water was found to have been liberated by our two experiments on epidotized dike samples. This finding is similar to that described by Coelho et al. (2015) in an experiment on a strongly chloritized metadiabase dike at high temperature (400–500 °C) in a Paterson apparatus using dry argon over ~30 h. Coelho et al. (2015) noticed that the chlorite in that sample had turned red and that its lattice *d*-spacing had increased during the experiments. Coelho et al. (2015) attributed these changes to oxidation of chlorite via dehydrogenation and dehydroxylation (e.g., Borggaard et al., 1982; Lempart et al., 2018) and suggested that the expansion of chlorite would reduce sample porosity. The samples CO-51-e and CO-51-s provided to us by Coelho et al. (2015) are epidosites rather than chloritized metadiabase but they still contain relict chlorite (e.g., Fig. 2). The chlorite in these samples may have undergone the same changes as described by Coelho et al. (2015) despite our shorter experimental duration of only ~2 h above 400 °C and despite the chlorite not having

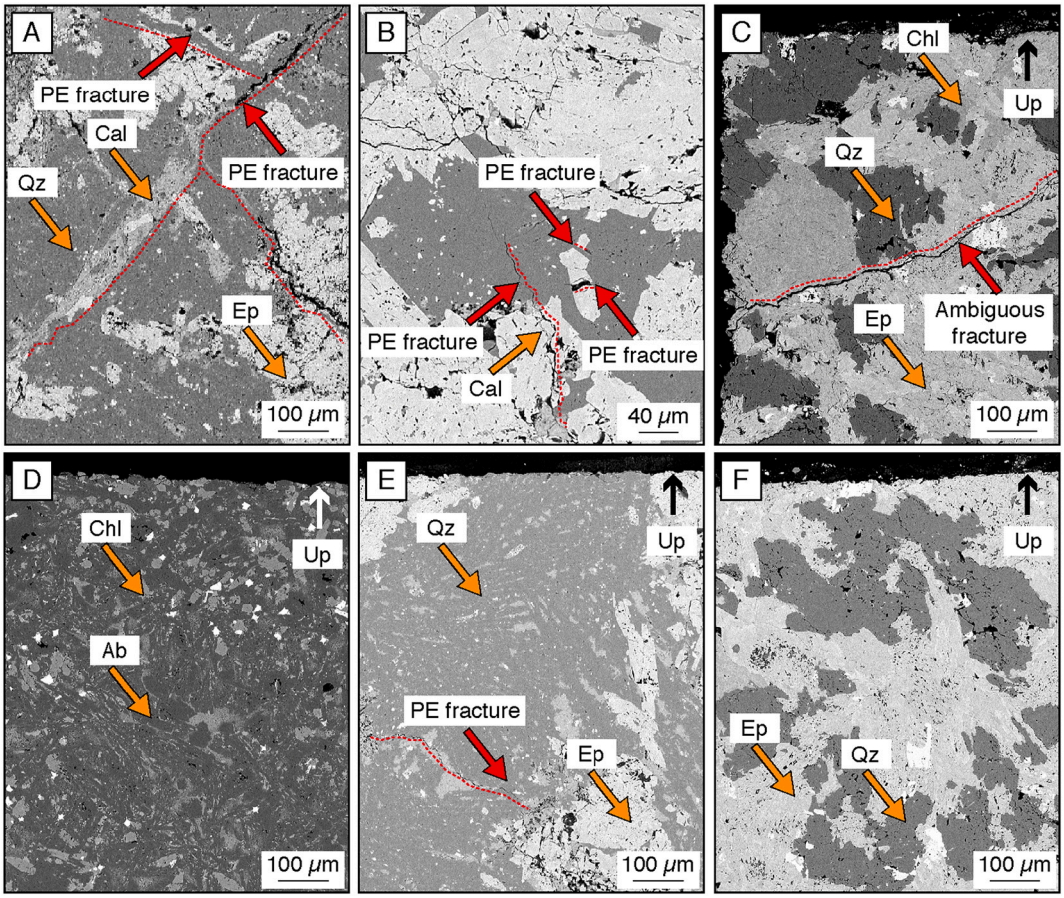

Fig. 6. Images in SEM-BSE mode of thin-sections cut through 15 mm mini-plugs following isobaric heating experiments. Pores appear black, fractures are indicated by red dotted lines and red arrows. (A), (B): Examples of pre-existing (PE) hydrothermal microfractures partly filled with calcite and quartz (sample SG14-56). (C) Example of ambiguous microfracture (sample CO-51-s). (D), (E), (F): Upper edges of the plugs (marked by vertical black and white arrows) that were in contact with the upper piston in the Paterson apparatus during permeability measurements. No new fractures formed along these edges during the experiments (spilite lava LD10-104-3 in D; epidosite lava SG14-56 in E; epidosite dike CO-51-s in F).

changed its macroscopic colour nor its optical properties in transmitted-light microscopy. In this scenario the chlorite would have liberated water irreversibly during initial heating, prior to the permeability measurements. Our Paterson apparatus has a controlled hot-spot over the length of the sample, but above and below the sample the apparatus is cooled such that temperature falls rapidly to room temperature. We therefore expect that the water evolved by chlorite would have rapidly diffused out of the sample owing to the Soret effect, and only condensed on the upper sample surface much later after the experiment had been terminated and the apparatus cooled. It is improbable that the liberated H_2O formed a water phase (separate from the argon) during the experiment and thereby induced a relative permeability effect, because the solubility of H_2O in argon at 50 MPa is very high, rising quickly from 25 mol% at 250 °C to 100% above the critical point of the Ar–H_2O system at 367 °C (Wu et al., 1990; Rigby and Prausnitz, 1968). Thus, the evolved H_2O would mix with the argon in the sample pores to form a single fluid phase, from which the H_2O would rapidly diffuse to the colder parts of the apparatus. No unusual features were noted in the amplitude ratio and phase offset during the subsequent permeability measurements, and so we infer that the liberation of H_2O by chlorite had no effect on our results. Indeed, the measured temperature–permeability trends recorded for the two epidosite dike samples are the same as that found for the epidosite lava (Fig. 5), although water was neither observed in this nor in the other two spilite experiments. We conclude that none of the thermally induced processes described above, i.e., pressure solution, precipitation of minerals and dehydrogenation–hydroxylation of chlorite, can explain the observed reduction of permeability upon heating.

The formation or growth of microfractures upon heating is known to increase permeability (e.g., Kozusnikova and Konečný, 2011; Liu et al., 2018; Mordensky et al., 2019; Shmonov et al., 1995; Sun et al., 2016). Thermally induced microfracturing has been observed in a few studies in real-time SEM experiments or by comparing high-resolution photographs before and after the experiments (Guo et al., 2017; Liu et al., 2018; Nahhas et al., 2019; Shmonov et al., 1995). Additionally, Yong and Wang (1980) found that heating of Westerly granite above 70 °C at atmospheric pressure induced acoustic emissions attributable to microcracking. In contrast, observations by SEM of three fresh basalt samples during heating to 715 °C revealed neither growth of pre-existing microfractures nor formation of new microfractures (Shmonov et al., 1995). Similarly, altered andesites experienced only minor increase in the abundance and length of microfractures after heating (Mordensky et al., 2019). Formation of new microfractures in our experiments is perhaps conceivable, as the heating rates we used (up to ~10 °C/min) were above the 2 °C/min rate recommended to minimize thermally induced cracking in granites at room pressure (Richter and Simmons, 1974 and references therein; Yong and Wang, 1980). However, we found no evidence for systematic formation of new microfractures in SEM images acquired after our temperature experiments (Fig. 6). The apparent lack of new thermally induced microfractures may be due to the high effective pressures (50 MPa) in our experiments. Instead, reversible closure of the long (> ~200 μm length), pre-existing cross-cutting microfractures in our samples (Fig. 6) upon heating and their reopening upon cooling, due to thermoelasticity of the surrounding mineral matrix, is a plausible explanation for our reproducible

temperature–permeability trends (Cooper and Simmons, 1977; Richter and Simmons, 1974; Gaunt et al., 2016).

Another mechanism that may contribute to lowering permeability upon heating is differential thermoelastic expansion of the minerals composing our samples. The minerals not only expand by different amounts upon heating at 50 MPa (Table A1), but they also undergo different anisotropic expansions along their crystallographic axes. As examples of anisotropy, igneous plagioclase and hydrothermal albite expand by 70% more along their *c*-axes than along their other axes (Tribaudino et al., 2010) and epidote shows a 77% difference (Diego Gatta et al., 2011). We suggest that anisotropic expansion could close a portion of pore throats upon heating, thereby reducing permeability even though the volume of the confined interstitial pores is increasing (Section 5.2.1). As bulk and anisotropic thermoelastic expansions are reversible thermodynamic properties, they conform to the observed reversibility of the temperature–permeability trends of our samples.

5.2.3. Non-systematic changes in permeability

Superimposed on the main permeability–temperature trend in Fig. A1 are the much smaller, non-systematic shifts in permeability, which occurred during and between our heating and cooling runs. These shifts include both decreases and increases in permeability (e.g., room temperature behavior in Fig. A1B) and therefore they are unlikely to reflect changes in sample properties. We attribute the changes to subtle variations in instrumental reproducibility between consecutive days of measurements, as we had to decompress the samples overnight for laboratory-safety reasons, then reestablish the experimental conditions for the heating–cooling runs on the following day. With values an order of magnitude lower than the main permeability–temperature trends, we consider these non-systematic changes negligible for the present study.

5.2.4. Comparison of temperature–permeability trends in altered and unaltered submarine basalts

The negative temperature–permeability correlation found in the present study is consistent with the overall trend found by Shmonov et al. (1995) in a fresh, submarine, massive flow basalt between 25 and 250 °C at effective pressures of 30, 50 and 120 MPa (Fig. 7). However, that sample exhibits small deviations in the trend over narrow temperature intervals (25–50 °C and 150–200 °C; Fig. 7). Furthermore, upon heating to 250 °C, the permeability drops by a factor of ~20, some 12 times more than that observed in the spilite and epidosite samples in this study (Fig. 7). The experiments of Aksyuk et al. (1992) on a different sample of fresh, submarine, massive flow basalt found a negative correlation between 25 and 100 °C, similar to our results, but a positive temperature–permeability correlation between 100 and 600 °C. Again, the overall change in permeability is vastly larger than that of our spilites and epidosites. Unfortunately, as only these two mutually contrasting studies on fresh basalts are available, no systematic comparison can be drawn with the behavior of our spilite and epidosite samples.

5.3. Temperature–permeability correlations

For applications such as coupled hydraulic–thermal–chemical simulations of hydrothermal alteration, correction functions for temperature can be derived from the average temperature–permeability correlations expressed by Eqs. (4) and (5). For example, permeabilities measured at 25 °C and at an effective pressure of ~50 MPa can be corrected as follows:

$$log(k_T)_{epidosite} = log(k_{25}) + 0.03780 - 0.00156T + 1.9155 \times 10^{-6}T^2 \quad (6)$$

$$log(k_T)_{spilite} = log(k_{25}) + 0.04261 - 0.00177T + 2.6251 \times 10^{-6}T^2 \quad (7)$$

where T is temperature between 25 and 450 °C, k_{25} is the permeability (m^2) measured at 25 °C, and k_T is the permeability (m^2) at the desired subscripted T at 50 MPa effective pressure. For permeabilities (k_{exp})

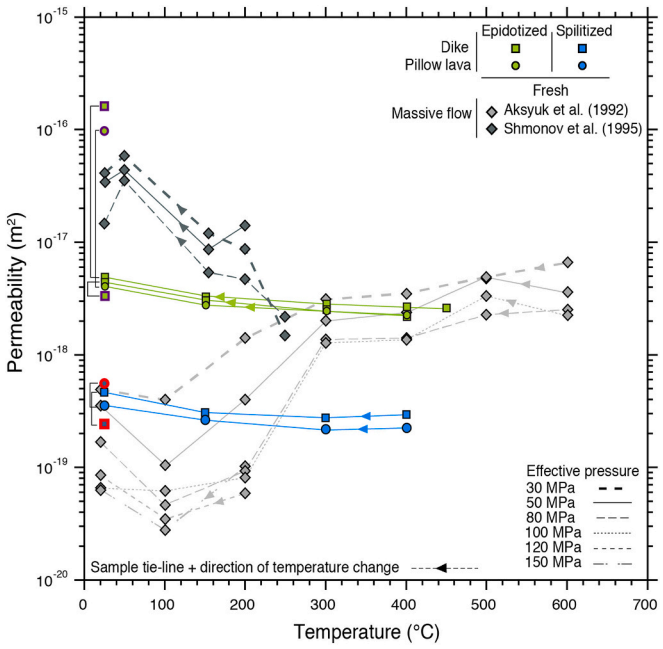

Fig. 7. Comparison of temperature–permeability trends along various isobars of effective pressure in fresh, submarine basaltic massive flows (Shmonov et al., 1995; Aksyuk et al., 1992) and in basalt dikes and lavas altered to spilite and epidosite (this study; 15 mm diameter mini-plugs). Room-temperature measurements at 55 MPa effective pressure on larger samples of spilites and epidosites (25 mm diameter plugs) are shown with thick red and purple outlines around symbols. Brackets indicate 25 °C measurements of 25 mm and 15 mm plugs from the same hand sample. (For interpretation of the references to colour in this figure legend, the reader is referred to the web version of this article.)

measured at an experimental temperature (T_{exp}) other than 25 °C, new values of the first polynomial coefficient a' can be determined by rearranging Eqs. (8) or (9), using the known k_{exp} and T_{exp}:

$$log(k_{exp})_{epidosite} = a' - 0.00156T_{exp} + 1.9155 \times 10^{-6}T_{exp}^2 \quad (8)$$

$$log(k_{exp})_{spilite} = a' - 0.00177T_{exp} + 2.6251 \times 10^{-6}T_{exp}^2 \quad (9)$$

The new a' values can then be inserted back into the Eqs. (8) or (9) with the desired high temperature in place of T_{exp} to calculate the corrected permeabilities (valid at 50 MPa effective pressure). Since these equations are based on only a few results, they would ideally be verified in the future with a larger dataset.

5.4. Influence of pressure on the temperature–permeability effect

Our experimental description of the temperature effect on permeability is strictly valid only for an effective pressure of 50 MPa. However, spilites and epidosites form at a variety of seawater depths and stratigraphic depths (Gilgen et al., 2016) and therefore in-situ pressures vary. A study on sandstones and shales (Guo et al., 2017) demonstrated that the magnitude of the temperature–permeability effect varies systematically with pressure: the absolute reduction in permeability is more pronounced at low effective pressures (5 MPa) than at high effective pressures (40 MPa). In the studies on fresh basalts by Aksyuk et al. (1992) and Shmonov et al. (1995), the data are too scattered to recognize a systematic relationship (Fig. 7). The quantitative correlation of the permeability of spilites and epidosites with pressure at elevated temperature therefore remains open. Until further studies become available, the trends in Fig. 4 provide first indications of the possible correlations. Fortunately, many experimental laboratories are able to measure room-temperature permeability routinely at the effective pressures typical of hydrothermal alteration in the oceanic crust.

5.5. P–T effects on permeability versus sample heterogeneity

We have demonstrated that increasing temperature to 450 °C reduces the permeability of spilites and epidosites by 40–50%, and increasing effective pressures by 35 to 55 MPa reduces permeability by 30–70% in epidosites and at least 50–80% in spilites. Are these changes significant compared to the natural variation in permeability of spilites and epidosites at the hand-specimen scale? Fig. 7 compares with brackets the room-temperature permeability at 25°C and ~50 MPa of 25 mm and 15 mm plugs drilled beside each other in the same hand samples (Fig. 3A). Among these duplicate measurements only the spilite pillow lava (LD10-104-3) and partially epidotized dike (CO-51-s) show similar permeabilities between the two plugs of different sizes. The duplicates of the other three samples (SG14-56, and CO-51-e) differ in permeability by 0.5–1.5 orders of magnitude. The spilitized dike (AB17-32C-spl) that was measured on a 25 mm plug and then re-cored and measured on the interior 15 mm plug (Fig. 3B) shows slightly different permeabilities. These differences between plugs from the same hand specimens show that permeability in our samples is highly heterogeneous at the centimeter scale. This is consistent with the 2–3 order of magnitude range in permeability of spilites and epidosites found in a larger dataset of spilites and epidosites from the Semail ophiolite (Brett et al., 2017). Thus, the changes in permeability upon heating to 450 °C and compressing to 50 MPa effective pressure are in fact only minor compared to the natural heterogeneity of permeability in typical spilites and epidosites. This conclusion is corroborated by the experiments of Coelho et al. (2015), who measured permeability on plugs from the same epidotised dike sample as our samples CO-51-e and CO-51-s using the steady-state flow method at 400 °C and 50 MPa. They obtained ~1.1×10^{-18} m^2 when using argon as the pore fluid and ~6.5×10^{-19} when using water. Both values are at least an order of magnitude lower than our measurements on 15 mm mini-plugs at the same *P–T* conditions. By contrast, the pressure–permeability effect from low pressure (5 MPa) to the high fluid pressures typical of hydrothermal alteration (33–55 MPa) is about twice that of the temperature–permeability effect at 50 MPa effective pressure.

6. Summary and conclusions

Our experiments have defined the first quantitative pressure–permeability and temperature–permeability trends for spilites and epidosites – two major types of high temperature, hydrothermally altered basalts in the oceanic crust. The experiments cover the range of in-situ *P–T* conditions in the most hydrothermally active portion of the crust: up to 55 MPa effective pressure at temperatures up to 450 °C.

At room temperature the permeabilities of spilites decrease by at least ~50–80% upon compression to 35 MPa effective pressure, and the permeabilities of epidosites decrease by up to ~70% upon compression to 55 MPa. The magnitudes and the smooth trends of the changes are similar to those previously reported for lower temperature, clay- and zeolite-altered basalts from present-day oceanic crust, and are attributed to the closure of pre-existing microcracks and pore space during compression. Heating the spilites and epidosites to 450 °C at 50 MPa effective pressure steadily lowers their permeabilities by ~40% and 50%, respectively, somewhat less than that caused by room-temperature compression to 55 MPa effective pressure.

Examination of the samples by SEM before and after the experiments revealed no new fractures caused by the heating and cooling runs. We therefore attribute the small decrease in permeability upon heating to two combined effects: (1) closure of the sparse pre-existing microfractures in the samples due to the bulk thermoelastic expansion of the crystalline rock-matrix, and (2) local restriction of throats between interstitial pores due to anisotropic mineral expansion. Cooling and heating cycles show that these changes are reversible.

Both the above pressure- and temperature-effects on permeability are small compared to the natural heterogeneity of permeability in spilites and epidosites at the centimeter scale. Further studies are required to confirm our temperature–permeability trends on a larger set of samples. However, in the interim, our results provide a convenient means to understand the changes in permeability of spilitized and epidotized dikes and pillows throughout the *P–T* realm in which much of the upper oceanic crust undergoes intensive water–rock interaction. The temperature effect can be readily incorporated into numerical simulations of hydraulic–thermal–chemical processes in the oceanic crust by means of our quantitative correlation Eqs. (6)–(9). In view of the small magnitude of the *P–T* effects, future studies aimed at providing input parameters for large-scale modelling should primarily focus on quantifying the highly heterogenous permeability of the volcanic crust.

Declaration of Competing Interest

The authors declare that they have no known competing financial interests or personal relationships that could have appeared to influence the work reported in this paper.

Acknowledgements

We gratefully acknowledge the logistical support during field work in the Sultanate of Oman by Khalid al-Tobi (Earth Secrets Co., Muscat) and Mohammed Al Araimi and Mohammed Al-Battashi (Public Authority for Mining, Muscat). Samuel Gilgen (University of Bern) assisted with sample collection in Oman, and Stanislas Sizaret (University of Orléans, France) kindly provided us with an epidosite sample from the Troodos ophiolite. We thank Stanislas Sizaret, two anonymous journal reviewers and Editor Philippe Agard for their helpful comments on this article. This work was supported by Swiss National Science Foundation (SNSF) Grants 200020-169653 and -188567 to L.W.D.

Appendix

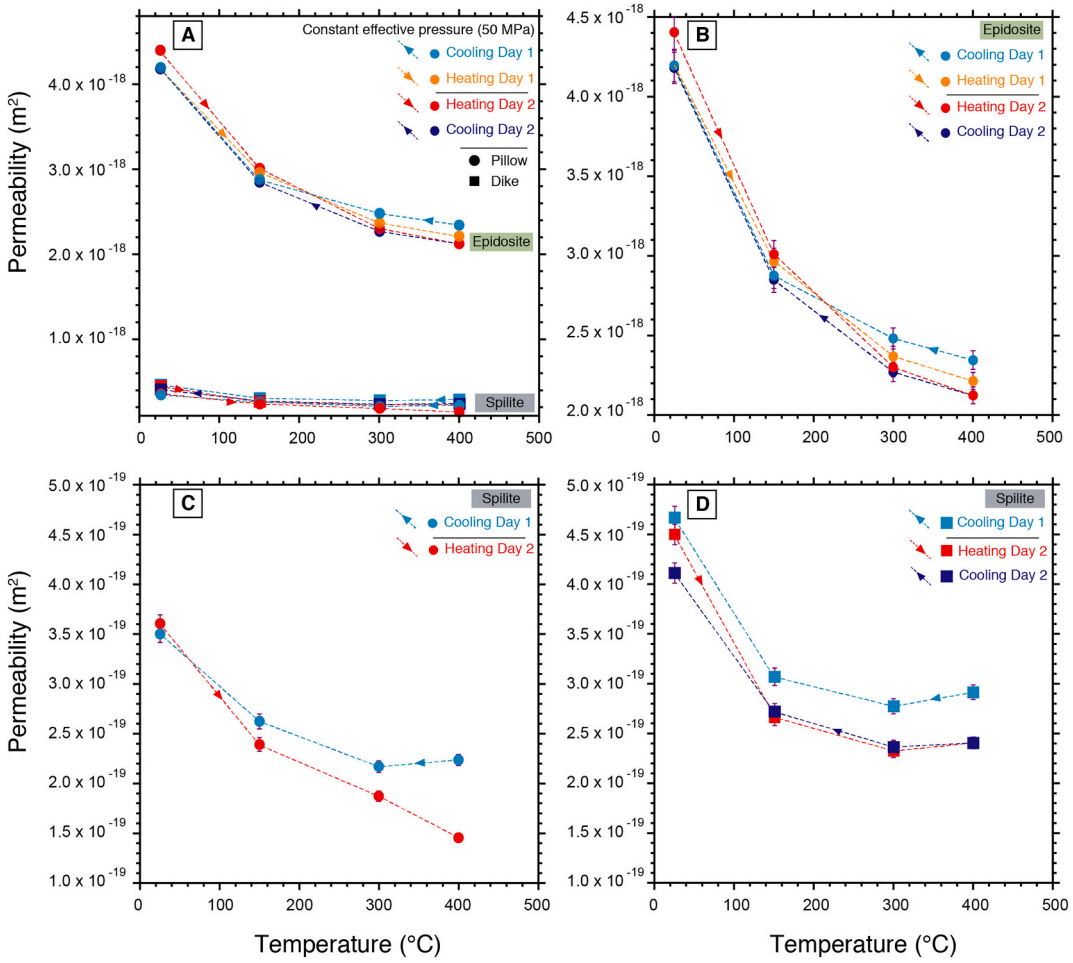

Fig. A1. Changes in permeability during repeated cooling–heating cycles at 50 MPa effective pressure. Analytical uncertainties shown in purple error bars (values in Table 4). The order of cooling and heating sequences follow the legend of each plot from top to bottom; arrowheads mark directions of temperature change. Pressure was reduced overnight between some cycles (see text for explanation). Scales in all plots are linear, not logarithmic. Scale range in (A) is different from (B); scale ranges are the same in (C) and (D). (A) Compilation of data from three samples: epidotized pillow lava SG15-56, spilitized pillow lava LD10-104-3 and spilitized dike AB17-32C-spl. (B) Permeabilities of epidotized pillow lava SG15-56 along two cooling–heating cycles. (C) Permeabilities of the spilitized pillow lava LD10-104-3 along cooling–heating cycles. (D) Permeabilities of the spilitized dike AB17-32C-spl along two cooling–heating cycles. (For interpretation of the references to colour in this figure legend, the reader is referred to the web version of this article.)

Table A1
Bulk thermoelastic expansion of spilite and epidosite minerals at 50 MPa.

Minerals	Molar volume[a] at 25 °C (cm^3/mol)	Molar volume[a] at 450 °C (cm^3/mol)	Absolute increase in molar volume between 25 and 450 °C (cm^3/mol)	Relative increase in molar volume between 25 and 450 °C (%)
Epidote	139.04	140.67	1.63	1.17
Quartz	22.88	23.22	0.34	1.48
Hematite	30.27	30.69	0.42	1.39
Titanite	55.62	56.17	0.54	0.97
Augite	73.28	75.47	2.19	2.99
Clinochlore	210.78	212.72	1.94	0.92
Albite	106.96	108.07	1.11	1.04

[a] Calculated from data in Holland and Powell (2011).

Appendix A. Supplementary data

Supplementary data to this article can be found online at https://doi.org/10.1016/j.tecto.2021.228994.

References

Aksyuk, A.M., Vitovtova, V.M., Pustovoy, A.A., Kharin, G.S., Shmonov, V.M., 1992. The permeability of oceanic basalts and some questions of the formation of hydrothermal springs in the rift zone of the Atlantic Ocean. Oceanol. Engl. Transl. 32, 1115–1122.

Alabaster, T., Pearce, J., 1985. The interrelationship between magmatic and ore-forming hydrothermal processes in the oman ophiolite. Econ. Geol. 80, 1–16. https://doi.org/10.2113/gsecongeo.80.1.1.

Anderson, R.N., Zoback, D.M., Hickman, S.H., Newmark, R.L., 1985. Permeability versus depth in the upper oceanic crust: in situ measurements in DSDP Hole 504B, eastern

equatorial pacific. J. Geophys. Res. 90, 3659–3669. https://doi.org/10.1029/JB090iB05p03659.
Bach, W., Peucker-Ehrenbrink, B., Hart, S.R., Blusztajn, J.S., 2003. Geochemistry of hydrothermally altered oceanic crust: DSDP/ODP Hole 504B - Implications for seawater-crust exchange budgets and Sr- and Pb-isotopic evolution of the mantle. Geochem. Geophys. Geosyst. 4, 1–29. https://doi.org/10.1007/s00269-010-0415-y.
Bakker, R.R., Violay, M.E.S., Benson, P.M., Vinciguerra, S.C., 2015. Ductile flow in sub-volcanic carbonate basement as the main control for edifice stability: New experimental insights. Earth Planet. Sci. Lett. 430, 533–541. https://doi.org/10.1016/j.epsl.2015.08.017.
Becker, K., 1989. Measurements of the permeability of the sheeted dikes in Hole 504B, ODP Leg 111. Proc. ODP, Sci. Results 111, 317–325. https://doi.org/10.2973/odp.proc.sr.111.156.1989.
Becker, K., Fisher, A.T., 2000. Permeability of upper oceanic basement on the eastern flank of the Endeavor Ridge determined with drill-string packer experiments. J. Geophys. Res. 105, 897–912. https://doi.org/10.1029/1999JB900250.
Belgrano, T.M., Diamond, L.W., Vogt, Y., Biedermann, A.R., Gilgen, S.A., 2019. A revised map of volcanic units in the Oman ophiolite: insights into the architecture of an oceanic proto-arc volcanic sequence. Solid Earth 10, 1181–1217. https://doi.org/10.5194/se-10-1181-2019.
Bernabé, Y., Mok, U., Evans, B., 2006. A note on the oscillating flow method for measuring rock permeability. Int. J. Rock Mech. Min. Sci. 43, 311–316. https://doi.org/10.1016/j.ijrmms.2005.04.013.
Borggaard, O.K., Lindgreen, H.B., Mørup, S., 1982. Oxidation and reduction of structural iron in chlorite at 480 °C. Clay Clay Miner. 30, 353–364. https://doi.org/10.1346/CCMN.1982.0300506.
Brett, A., Diamond, L.W., Gilgen, S.A., 2017. Deep flow paths in VMS systems: porosity and permeability of epidosite alteration in the Semail ophiolite, Oman. In: Proceedings of the 14th Biennial SGA Meeting, Quebéc, Canada, 2. The Society for Geology Applied to Mineral Deposits (SGA), pp. 661–664. https://numerique.banq.qc.ca/patrimoine/details/52327/3081324?docref=FH82G97UVOxAYi19lAiyiQ.
Cann, J.R., 1969. Spilites from the Carlsberg Ridge, Indian Ocean. J. Petrol. 10, 1–19. https://doi.org/10.1093/petrology/10.1.1.
Christensen, N.I., Ramananantoandro, R., 1988. Permeability of the oceanic crust based on experimental studies of basalt permeability at elevated pressures. Tectonophysics 149, 181–186. https://doi.org/10.1016/0040-1951(88)90126-6.
Christensen, N.I., Smewing, J.D., 1981. Geology and seismic structure of the northern section of the Oman ophiolite. J. Geophys. Res. 86, 2545–2555. https://doi.org/10.1029/JB086iB04p02545.
Coelho, G., Branquet, Y., Sizaret, S., Arbaret, L., Champallier, R., Rozenbaum, O., 2015. Permeability of sheeted dykes beneath oceanic ridges: strain experiments coupled with 3D numerical modeling of the Troodos Ophiolite, Cyprus. Tectonophysics 644, 138–150. https://doi.org/10.1016/j.tecto.2015.01.004.
Cooper, H.W., Simmons, G., 1977. The effect of cracks on the thermal expansion of rocks. Earth Planet. Sci. Lett. 36, 404–412. https://doi.org/10.1016/0012-821X(77)90065-6.
Diego Gatta, G., Merlini, M., Lee, Y., Poli, S., 2011. Behavior of epidote at high pressure and high temperature: a powder diffraction study up to 10 GPa and 1,200 K. Phys. Chem. 38, 419–428. https://doi.org/10.1007/s00269-010-0415-y.
Faulkner, D.R., Rutter, E.H., 2000. Comparisons of water and argon permeability in natural clay-bearing fault gouge under high pressure at 20°C. J. Geophys. Res. Solid Earth 105, 16415–16426. https://doi.org/10.1029/2000JB900134.
Fischer, G.J., 1992. The determination of permeability and storage capacity: pore pressure oscillation method. In: Evans, B., Wong, T. (Eds.), Fault Mechanics and Transport Properties of Rocks, , 1st editionVol. 51. Academic Press, Cambridge, MA, pp. 187–211. https://doi.org/10.1016/S0074-6142(08)62823-5.
Fisher, A.T., 1998. Permeability within basaltic ocean crust. Rev. Geophys. 36, 143–182. https://doi.org/10.1029/97RG02916.
Fortin, J., Stanchits, S., Vinciguerra, S., Gueguen, Y., 2011. Influence of thermal and mechanical cracks on permeability and elastic wave velocities in a basalt from Mt. Etna volcano subjected to elevated pressure. Tectonophysics 503, 60–74. https://doi.org/10.1016/j.tecto.2010.09.028.
Galley, A.G., Bailes, A.H., Kitzler, G., 1993. Geological setting and hydrothermal evolution of the Chisel Lake and North Chisel Zn-Pb-Cu-Ag-Au massive sulfide deposits, Snow Lake, Manitoba. Explor. Min. Geol. 2, 271–295.
Gaunt, H.E., Sammonds, P.R., Meredith, P.G., Chadderton, A., 2016. Effect of temperature on the permeability of lava dome rocks from the 2004-2008 eruption of Mount St. Helens. Bull. Volcanol. 78, 30. https://doi.org/10.1007/s00445-016-1024-5.
Gilbert, L.A., Bona, M.L., 2016. Permeability of oceanic crustal rock samples from IODP Hole 1256D. Geochem. Geophys. Geosyst. 17, 3825–3832. https://doi.org/10.1002/2016GC006467.
Gilbert, L.A., Salisbury, M.H., 2011. Oceanic crustal velocities from laboratory and logging measurements of Integrated Ocean Drilling Program Hole 1256D. Geochem. Geophys. Geosyst. 12, Q09001 https://doi.org/10.1029/2011GC003750.
Gilgen, S.A., Diamond, L.W., Mercolli, I., 2016. Sub-seafloor epidosite alteration: timing, depth and stratigraphic distribution in the Semail Ophiolite, Oman. Lithos 260, 191–210. https://doi.org/10.1016/j.lithos.2016.05.014.
Gillis, K.M., Banerjee, N.R., 2000. Hydrothermal alteration patterns in supra-subduction zone ophiolites. Geol. Soc. Am. Spec. 349, 283–298. https://doi.org/10.1130/0-8137-2349-3.283.
Gillis, K.M., Robinson, P.T., 1990. Patterns and processes of alteration in the lavas and dykes of the Troodos Ophiolite, Cyprus. J. Geophys. Res. Solid Earth 95, 21523–21548. https://doi.org/10.1029/JB095iB13p21523.
Guo, X., Zou, G., Wang, Y., Wang, Y., Gao, T., 2017. Investigation of the temperature effect on rock permeability sensitivity. J. Pet. Sci. Eng. 156, 616–622. https://doi.org/10.1016/j.petrol.2017.06.045.
Hannington, M.D., 2014. Volcanogenic massive sulfide deposits. In: Holland, H.D., Turekian, K.K. (Eds.), Treatise on Geochemistry, 2nd edition. Elsevier, Oxford, pp. 463–488.
Hannington, M.D., Santaguida, F., Kjarsgaard, I.M., Cathles, L.M., 2003. Regional-scale hydrothermal alteration in the Central Blake River Group, western Abitibi subprovince, Canada: Implications for VMS prospectivity. Mineral. Deposita 38, 393–422. https://doi.org/10.1007/s00126-002-0298-z.
Hasenclever, J., Theissen-Krah, S., Rüpke, L.H., Morgan, J.P., Iyer, K., Petersen, S., Devey, C.W., 2014. Hybrid shallow on-axis and deep off-axis hydrothermal circulation at fast-spreading ridges. Nature 508, 508–512. https://doi.org/10.1038/nature13174.
Holland, T.J.B., Powell, R., 2011. An improved and extended internally consistent thermodynamic dataset for phases of petrological interest, involving a new equation of state for solids. J. Metamorph. Geol. 29, 333–383. https://doi.org/10.1111/j.1525-1314.2010.00923.x.
Honarpour, M., Koederitz, L., Harvey, A.H., 1986. Measurement of rock relative permeability. In: Relative Permeability of Petroleum Reservoirs. CRC Press, Boca Raton, Florida, pp. 1–12.
Jarrard, R.D., Abrams, L.J., Pockalny, R., Larson, R.L., Hirono, T., 2003. Physical properties of upper oceanic crust: Ocean Drilling Program Hole 801C and the waning of hydrothermal circulation. J. Geophys. Res. Solid Earth 108, 1–26. https://doi.org/10.1029/2001JB001727.
Johnson, D.M., 1980. Fluid permeability of oceanic basalts. Initial Rep. Deep Sea Drill. Proj. 68, 1473–1477.
Jowitt, S.M., Jenkin, G.R.T., Coogan, L.A., Naden, J., 2012. Quantifying the release of base metals from source rocks for volcanogenic massive sulfide deposits: effects of protolith composition and alteration mineralogy. J. Geochem. Explor. 118, 47–59. https://doi.org/10.1016/j.gexplo.2012.04.005.
Karato, S., 1983. Physical properties of basalts from Deep Sea Drilling Project Hole 504B, Costa Rica Rift. Initial Rep. Deep Sea Drill. Proj. 69, 687–695.
Kozusnikova, A., Konečný, P., 2011. Influence of temperature on the permeability of rocks. Geotechnique 61, 1081–1085. https://doi.org/10.1680/geot.8.T.034.
Kranz, R.L., Saltzman, J.S., Blacic, J.D., 1990. Hydraulic diffusivity measurements on laboratory rock samples using an oscillating pore pressure method. Int. J. Rock Mech. Min. Sci. 27, 345–352. https://doi.org/10.1016/0148-9062(90)92709-N.
Kusano, Y., Umino, S., Shinjo, R., Ikei, A., Adachi, Y., Miyashita, S., Arai, S., 2017. Contribution of slab-derived fluid and sedimentary melt in the incipient arc magmas with development of the paleo-arc in the Oman Ophiolite. Chem. Geol. 449, 206–225. https://doi.org/10.1016/j.chemgeo.2016.12.012.
Kushnir, A.R.L., Martel, C., Champallier, R., Wadsworth, F.B., 2017. Permeability evolution in variably glassy basaltic andesites measured under magmatic conditions. Geophys. Res. Lett. 44 (10), 262–10,271. https://doi.org/10.1002/2017GL074042.
Lempart, M., Derkowski, A., Luberda-Durnaś, K., Skiba, M., Błachowski, A., 2018. Dehydrogenation and dehydroxylation as drivers of the thermal decomposition of Fe-chlorites. Am. Mineral. 103, 1837–1850. https://doi.org/10.2138/am-2018-6541.
Liu, J., Li, B., Tian, W., Wu, X., 2018. Investigating and predicting permeability variation in thermally cracked dry rocks. Int. J. Rock Mech. Min. Sci. 103, 77–88. https://doi.org/10.1016/j.ijrmms.2018.01.023.
Mordensky, S.P., Kennedy, B.M., Villeneuve, M.C., Lavallée, Y., Reichow, M.K., Wallace, P.A., 2019. Increasing the permeability of hydrothermally altered andesite by transitory heating. Geochem. Geophys. Geosyst. 20, 5251–5269. https://doi.org/10.1029/2019GC008409.
Mottl, M.J., Wheat, G.C., 1994. Hydrothermal circulation through mid-ocean ridge flanks: fluxes of heat and magnesium. Geochim. Cosmochim. Acta 58, 2225–2237. https://doi.org/10.1016/0016-7037(94)90007-8.
Nahhas, T., Py, X., Sadiki, N., 2019. Experimental investigation of basalt rocks as storage material for high-temperature concentrated solar power plants. Renew. Sust. Energ. Rev. 110, 226–235. https://doi.org/10.1016/j.rser.2019.04.060.
Nara, Y., Meredith, P.G., Yoneda, T., Kaneko, K., 2011. Influence of macro-fractures and micro-fractures on permeability and elastic wave velocities in basalt at elevated pressure. Tectonophysics 503, 52–59. https://doi.org/10.1016/j.tecto.2010.09.027.
Nehlig, P., 1994. Fracture and permeability analysis in magma-hydrothermal transition zones in the Samail ophiolite (Oman). J. Geophys. R. 99, 589–601. https://doi.org/10.1029/93JB02569.
Osozawa, S., Shinjo, R., Lo, C.H., Jahn, B.M., Hoang, N., Sasaki, M., Wakabayashi, J., 2012. Geochemistry and geochronology of the Troodos ophiolite: an SSZ ophiolite generated by subduction initiation and an extended episode of ridge subduction? Lithosphere 4, 497–510. https://doi.org/10.1130/L205.1.
Paterson, M.S., 1970. A high-pressure, high-temperature apparatus for rock deformation. Int. J. Rock Mech. Min. Sci. 7, 517–526. https://doi.org/10.1016/0148-9062(70)90004-5.
Patten, C.G.C., Pitcairn, I.K., Teagle, D.A.H., Harris, M., 2016. Sulphide mineral evolution and metal mobility during alteration of the oceanic crust: Insights from ODP Hole 1256D. Geochim. Cosmochim. Acta 193, 132–159. https://doi.org/10.1016/j.gca.2016.08.009.
Pezard, P.A., 1990. Electrical properties of mid-oceanic ridge basalt and implication for the structure of the upper oceanic crust in Hole 504B. J. Geophys. Res. 95, 9237–9264. https://doi.org/10.1029/JB095iB06p09237.
Richardson, C.J., Cann, J.R., Richards, H.G., Cowan, J.G., Siegel, J., 1987. Metal-depleted root zones of the Troodos ore-forming hydrothermal systems, Cyprus. Earth Planet. Sci. Lett. 84, 243–253. https://doi.org/10.1097/Ol.ta.0000220385.34197.f9.

Richter, L., Diamond, L.W., 2019. Identifying deep hydrothermal fluids that leach metals from the oceanic crust and generate seafloor VMS deposits. In: Proceedings of the 15th SGA Biennial Meeting, Glasgow, Scotland. The Society for Geology Applied to Mineral Deposits (SGA), 1, pp. 76–79.

Richter, D., Simmons, G., 1974. Thermal expansion behavior of igneous rocks. Int. J. Rock Mech. Min. Sci. 11, 403–411. https://doi.org/10.1016/0148-9062(74)91111-5.

Rigby, M., Prausnitz, J.M., 1968. Solubility of water in compressed nitrogen, argon, and methane. J. Phys. Chem. 72, 330–334. https://doi.org/10.1021/j100847a064.

Seyfried, W.E., Berndt, M.E., Seewald, J.S., 1988. Hydrothermal alteration processes at mid-ocean ridges; constraints from diabase alteration experiments, hot-spring fluids and composition of the oceanic crust. Can. Mineral. 26, 787–804.

Shmonov, V.M., Vitovtova, V.M., Zarubina, I.V., 1995. Permeability of rocks at elevated temperatures and pressures. In: Shmulovich, K.I., Yardley, B.W.D., Gonchar, G.G. (Eds.), Fluids in the Crust: Equilibrium and Transport Properties. Springer, Netherlands, Dordrecht, pp. 285–313. https://doi.org/10.1007/978-94-011-1226-0_11.

Staudigel, H., 2014. Chemical fluxes from hydrothermal alteration of the oceanic crust. In: Holland, H.D., Turekian, K.K. (Eds.), Treatise on Geochemistry, , 2nd editionvol. 4. Elsevier, Oxford, pp. 583–603. https://doi.org/10.1016/B978-0-08-095975-7.00318-1.

Sun, Y.Z., Xie, L.Z., He, B., Gao, C., Wang, J., 2016. Effects of effective stress and temperature on permeability of sandstone from CO_2-plume geothermal reservoir. J. Rock Mech. Geotech. Eng. 8, 819–827. https://doi.org/10.1016/j.jrmge.2016.07.004.

Tegeler, R.S., Wagner, W., 1999. A new equation of state for argon covering the fluid region for temperatures from the melting line to 700 K at pressures up to 1000 MPa. J. Phys. Chem. Ref. Data 28, 779–850. https://doi.org/10.1063/1.556037.

Tribaudino, M., Angel, R.J., Cámara, F., Nestola, F., Pasqual, D., Margiolaki, I., 2010. Thermal expansion of plagioclase feldspars. Contrib. Mineral. Petrol. 160, 899–908. https://doi.org/10.1007/s00410-010-0513-3.

van Everdingen, D.A., 1995. Fracture characteristics of the sheeted dike complex, Troodos ophiolite, Cyprus: implications for permeability of oceanic crust. J. Geophys. Res. 100, 19957–19972. https://doi.org/10.1029/95JB01575.

Varga, R.J., Gee, J.S., Bettison-Varga, L., Anderson, R.S., Johnson, C.L., 1999. Early establishment of seafloor hydrothermal systems during structural extension: paleomagnetic evidence from the Troodos ophiolite, Cyprus. Earth Planet. Sci. Lett. 171 (2), 221–235. https://doi.org/10.1016/S0012-821X(99)00147-8.

Violay, M., Pezard, P.A., Ildefonse, B., Belghoul, A., Laverne, C., 2010. Petrophysical properties of the root zone of sheeted dikes in the ocean crust: a case study from Hole ODP/IODP 1256D, Eastern Equatorial Pacific. Tectonophysics 493, 139–152. https://doi.org/10.1016/j.tecto.2010.07.013.

Wu, G., Heilig, M., Lentz, H., Franck, E.U., 1990. High pressure phase equilibria of the water-argon system. Ber. Bunsenges. Phys. Chem. 94, 24–27. https://doi.org/10.1002/bbpc.19900940106.

Yong, C., Wang, C., 1980. Thermally induced acoustic emissions in Westerly Granite. Geophys. Res. Lett. 7, 1089–1092. https://doi.org/10.1029/GL007i012p01089.

Zaraisky, G.P., Balashov, V.N., 1995. Thermal decompaction of rocks. In: Shmulovich, K.I., Yardley, B.W.D., Gonchar, G.G. (Eds.), Fluids in the Crust: Equilibrium and Transport Properties. Springer, Netherlands, pp. 253–284. https://doi.org/10.1007/978-94-011-1226-0_10.